INTERNATIONAL JOURNAL OF AUTOMOTIVE AND MECHANICAL ENGINEERING (IJAME)
ISSN: 2229-8649 e-ISSN: 2180-1606
VOL. 18, ISSUE 2, 8781 – 8789
DOI: https://doi.org/10.15282/ijame.18.2.2021.16.0672

ORIGINAL ARTICLE

Experimental Investigations on Microwave-Current Assisted Sintering Process and Oxidation of Graphite Die at High Temperature

H.K.M. Al-Jothery[1,2*], T.M.B. Albarody[1], P.S.M. Megat-Yusoff[1], N. Al-Shaibani[1] and H.G. Mohammed[1]

[1]Mechanical Engineering Department, Universiti Teknologi PETRONAS, 32610 Seri Iskandar, Perak, Malaysia
Phone: +60175655432, +9647707224241
[2]Mechanical Engineering Department, University of Al-Qadisiyah, 58001 Al-Diwaniyah, Qadisiyah, Iraq

ABSTRACT – In the current-assisted sintering technique, graphite is mainly used to fabricate die and other components (such as electrodes and spacers) because of its excellent thermoelectric properties, high melting point and high ratio of the tensile strength to the compressive strength. As widely known, graphite is one of the brittle materials, and the failure is difficult to be anticipated before it happens. Besides, there is a lack of information about the effects of sintering process, environment and impurity on the graphite structure of the furnace, especially the die, which is the weakest part of the graphite structure. Therefore, the effects of electrical field and oxidation on the graphite die of microwave-current assisted sintering apparatus were investigated at a high temperature of 600-1900 °C based on physical characteristics and mechanical strength. In this article, the spark discharge phenomenon was experimentally proved during the sintering process of nonconductive material. The tensile strength of the upper punch after the sintering process was 20.2% higher than the pristine one because of the transforming of micro-graphite to carbon nanotubes which increased with increasing the temperature. On the other hand, the tensile strengths of graphite lower punch and sleeve were slightly dropped. While, the oxidation of GW-6S graphite in the air caused a mass loss that led to the reduction in tensile and compressive strengths.

ARTICLE HISTORY
Received: 8th Sept 2020
Revised: 3rd Mar 2021
Accepted: 16th June 2021

KEYWORDS
Electrical-assisted sintering technique;
Graphite die;
Graphite oxidation;
Mechanical strength;
High temperature

INTRODUCTION

Electrical-assisted sintering technique (EAST) is a promising novel sintering technique using (pulsed/ non-pulsed) direct current to achieve a rapidly good consolidation of (conductive/ nonconductive) powder for producing a sintered part by generated heat and applied pressure [1, 2]. In this decade, there are few EAST have been developed. Generally, they are spark plasma sintering (SPS), flash sintering (FS) and flash spark plasma sintering (FSPS) techniques [3-8]. For sintering process of silicon carbide (SiC) using SPS technique, the current will not pass through the powders because of the negative temperature coefficient of resistance (NTCR) below 1000 °C. Forcing the current to pass through SiC without heating causes a rapid increase in temperature and an uncontrollable electrical current in SiC [9]. Therefore, the current heated the graphite die elements and the temperature of nonconductive SiC powder will be increased [10-12].

Graphite mould elements have widely been used in CAS techniques [13-16], as well as the hot pressing sintering technique [17-19]. This is because graphite is a moderating material at high temperature and has high thermal and electrical conductivities [20, 21]. In addition, it has good corrosion resistance, high chemical stability, and easy to be machined, but the mechanical strength of graphite sharply deteriorates in the oxidiser environment. On the other hand, graphite material has a low tensile strength (≈ 30 MPa), which is less than its compression strength (where value of compression strength is only three times tensile strength at the centre of disc specimen) [22]. Because of that, few researchers have attempted to use another material to fabricate die elements for higher pressure applied during the sintering process. For instance, Grasso et al. have conducted SPS of pure Alumina powder under an applied pressure of 500 MPa using tungsten carbide (WC) die to fulfil a highly transparent sample at <1200 °C [23]. Also, they made low cost die for high pressure (>400 MPa) SPS sintering from carbon fibre composite (CFC) comparing with WC die [24]. Then, electrically conductive silicon carbide (ECSiC) has been used to fabricate die elements for high-pressure SPS sintering to achieve lower sintering temperature. The graphite, WC and CFC dies have a high electrical conductivity at high temperature compared with the ECSiC die. While, the ECSiC, WC and CFC dies limited the sintering temperature below 1600 °C. However, there is no candidate material to replace the graphite die in CAS apparatus for sintering the ultra-high temperature materials; melting point is above 2000 °C. Therefore, the deterioration of graphite' mechanical properties due to a little oxidation in the extreme condition is not well known.

Graphite has been defined as a porous media. For the graphite oxidation of air, there are three regimes based on the temperature limits. The first one is a chemical regime, when the temperature is below 500 °C. The second regime is in-pore diffusion-controlled, when the temperature ranged between 500 °C and 900 °C. The third regime is the boundary layer, when the temperature is above 900 °C [25]. Blanchard studied the oxidation of graphite and gave another setting of is in-pore diffusion-controlled regime between 600 °C and 900 °C. Moreover, there are five parameters that influence

*CORRESPONDING AUTHOR | H.K.M. Al-Jothery | ✉ husam_16005123@utp.edu.my

the transition temperature of oxidation regimes, which are density, impurity, flow rate, size and microstructure of graphite specimen [26, 27].

In this paper, we report the effect of MCAS process on the graphite mould by testing the tensile strength of the mould components after the process. Besides, the physical and thermal characteristics of carbon nanotubes (CNTs) were investigated. On the other hand, the behaviour of GW-6S graphite oxidation was reported at variant temperature and time. Moreover, the oxidation effect of GW-6S graphite on tensile strength and compressive strength based on mass loss percentage was carried out to predict the service life of graphite mould in the MCAS apparatus.

EXPERIMENTAL METHODOLOGY

Materials

Graphite material (GW-6S) was supplied by Beijing Great Wall Co., Ltd, China. The graphite electrodes were directly designed and implemented by the Beijing Great Wall Company with dimensions of 150×40 mm. The die elements were designed by the authors and implemented by Kaizen design solutions company, Malaysia. The dimensions of the graphite cylindrical sleeve were 30×8 mm, and the hole was 13 mm. Besides, the graphite punches dimensions are 25×13 mm, see Figure 1. A nonconductive silicon carbide nanopowder used in this work is a cubic type. The purity of that supplied cubic silicon carbide nanopowder is >98% purity and was purchased from Hong Wu International Group Ltd, China. The average particle size of the nanopowder is 70 nm.

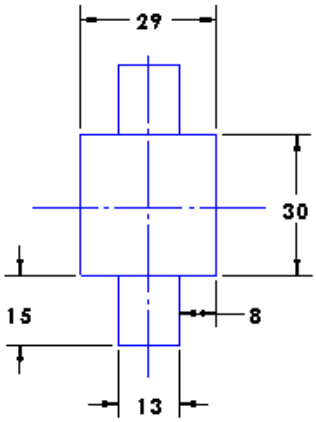

Figure 1. 2D drawing of graphite die.

Structure of Graphite Components

The core of MCAS furnace is a symmetrical assembly GW-6S graphite structure for facilitating the sintering process and ensuring thermal distribution to be approximately equal around the powder. It consists of two graphite blocks, two graphite rods, two punches and a cylindrical mould. The graphite blocks of 100×100×50 mm were machined for connecting to the graphite rods (upper and lower). They were outside the cavity of the furnace and connected to the high direct current power supply. The mould was placed between those graphite rods which were connected to two graphite punches (upper punch is the anode and lower one is a cathode) and subjected to microwave (MW) radiation. All surfaces in contact with the compacted SiC sample were lined with graphite foil of 0.1 mm thickness to prevent the sinterability between the components of graphite die and compacted SiC nanopowder, as well as aid in the sintered sample removal.

Heating Process

DC power supply (SAW POWER 1500 DC, Malaysia WIM) was used to generate heating in the mould based on joule heating. Argon gas was used during the heating process to prevent oxidation and reduce the thermal convection to the cavity of the furnace. The flow rate of the argon gas was 0.5 L/min and controlled by a flow valve. Also, the applied pressure of 20 MPa was fully maintained to the compacted SiC powder. A PID controller (RKC PF900 EMC SDN BHD, Malaysia) was used to control the electrical current following a temperature diagram. The non-contact infrared thermometer laser was used to measure the surface temperature of the graphite sleeve. That process was performed at different temperatures from 600 °C to 1900 °C (step of 100 °C) for testing the components of graphite die. Thus, the components of graphite die were freely cooled under an argon atmosphere. The oxidation of graphite based on the effect of time was figured out following the above heating procedure under atmospheric pressure. The samples were exposed to the airflow with dwelling time from 1 min to 8 min (step of 1 min). The airflow was 0.2 L/min for activating oxidation energy. Then, the samples were freely cooled under ambient conditions. Moreover, the above oxidation procedure was repeated for oxidising the graphite under atmospheric pressure and soaking time 40 min. The graphite electrodes were protected using a high density of assembly alumina tube and argon gas during the oxidation process.

Physical Characteristics and Mechanical Strength

For microstructure characterisation of CNTs sample, the lower surface of upper graphite punch was cut in the depth of 1 mm using a precision wheel cutter. Then, the graphite pellet was cleaned for scanning and imaging the lower surface

of the pellet. Crystalline characterisation of CNTs sample was carried out by x-ray diffraction machine (XRD, Model X'Pert3 Powder, Malvern PANalytical) with Cu K-α and λ=1.540598 Å. XRD data were obtained over 2θ range from 20° to 60° with a step size of 0.05°. The associated analysis of XRD data was figured out using X'Pert HighScore Plus v3.0 (Malvern PANalytical, UK). Then, the polishing of CNTs sample was carried out for FE-SEM test (MetaServ-250 Twin Grinder-Polisher, US BUEHLER) using 1 μm suspended polycrystalline diamond liquid and diamond extender with a high napped polishing pad (Metallographic, US PACE TECHNOLOGIES). The morphology of the polished sample was verified by Field-Emission Scanning Electron Microscope (FE-SEM, Model Supra 55VP, Carl Zeiss AG).

The average crystallite size of CNTs was estimated using the XRD profile via Scherrer's formula and verified by FESEM.

$$D = \frac{K\lambda}{B(2\theta)\,\mathrm{Cos}(\theta)} \tag{1}$$

$$d = \frac{n\lambda}{2\mathrm{Sin}(\theta)} \tag{2}$$

where K represents the Scherrer's factor which is dimensionless (0.91), λ represents the x-ray wavelength, B(2θ) presents the full width at half maximum (FWHM) corresponding to the diffraction peak in radian (after subtracting the line broadening of XRD instrument), and θ is the Bragg angle of diffraction peak. The interlayer spacing, or lattice spacing, d, was calculated using the XRD pattern via Bragg's law, as shown in Eq. (2), where n is an integer.

A thermal gravimetric analyser (TGA) was used to conduct the oxidation of graphite and CNTs samples (Perkin Elmer Pyris1 TGA, USA). The specimens were a thin disc with d= 13 mm. The samples were heated up from room temperature to 900 °C with a specified heating rate of 25 °C/min under air atmosphere. The weight of the graphite die (after/before heating) was measured using a digital balance machine. Moreover, the ring compression test [28, 29] of graphite samples was performed to measure the tensile strength using a compression test machine (Model ADR Touch SOLO A0034, US ELE) [30]. The mechanical tests were repeated three times at each temperature to ensure the test and measured data and confirm the reproducibility; then, the average reads were taken as a result [31].

RESULTS AND DISCUSSION

Figure 2 shows the sleeve before and after the sintering process. The surface of the graphite sleeve after the sintering process is rougher than the one before the sintering process. Figure 3 shows the effect of the sintering process on the tensile strength of the die components (upper punch, lower punch and sleeve) at variant temperatures. The tensile strength of graphite sleeve and lower punch (cathode) has a small drop with increasing temperature. This is because of the impurity of graphite material and inert gas, which cause oxidation of graphite die. Clearly, oxidation increased with increasing temperature due to the increase in the chemical rate that proportional to rising temperature [32]. Besides, the dropping in mechanical strength of the sleeve is higher than the dropping in mechanical strength of the cathode because the surface area of sleeve is higher than the one of cathode. The oxidation increased when the surface area was increasing at high temperature [33]. On the other hand, the graph's behaviour of anode can be divided into two parts. In the first part, when the temperature below 1100 °C, the tensile strength is decreasing when the temperature is increasing (follows the same pattern of the cathode and sleeve). In the second part, when the temperature is above 1100 °C, the tensile strength increases when temperature increases because the formation of CNTs is continuously growing when temperature increases [34].

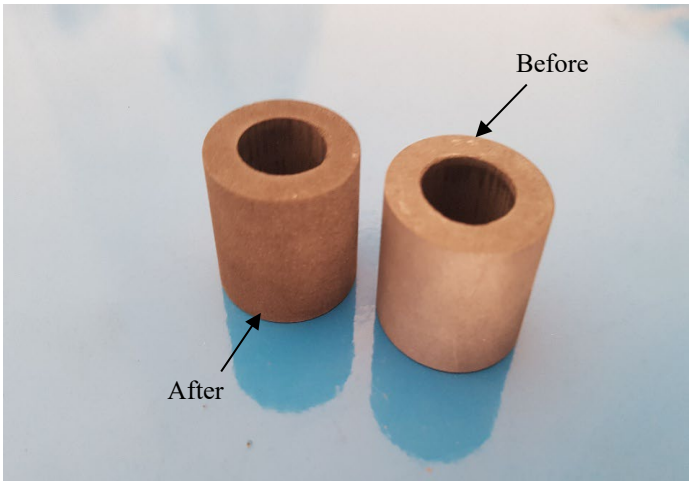

Figure 2. The graphite sleeve before and after the sintering process.

At 1900 °C, the tensile strength of specimen is 20.2% higher than the tensile strength of the pristine one because the mechanical strength of CNTs is higher than the mechanical strength of graphite [35, 36]. This led us to investigate deeper into the graphite anode using physical tests (such as XRD, FESEM and TGA), and we found that CNTs formed on the

lower face of the anode, as shown in Figure 4. The formation of CNTs was probably occurred due to the spark discharge phenomenon between the two graphite punches through the SiC powder during the sintering process of MCAS, which is another way to prove that phenomenon. Figure 4 shows CNTs formed in each grain of graphite and carbonaceous network between the grains of graphite, which enhances the mechanical properties. So, the tensile strength of graphite anode is proportional with the temperature above 1200 °C because SiC can be conducted at a temperature above 1000 °C; that leads to allowing the current to pass through the compacted powder to generate spark. However, the impact of CNTs transformation of the lower face of anode starts at 1300 °C. Also, the formation of CNTs is proportional with temperature [37] during spark discharge. Therefore, the tensile strength of anode was improved because of CNTs which have excellent mechanical properties compared with graphite [35, 38].

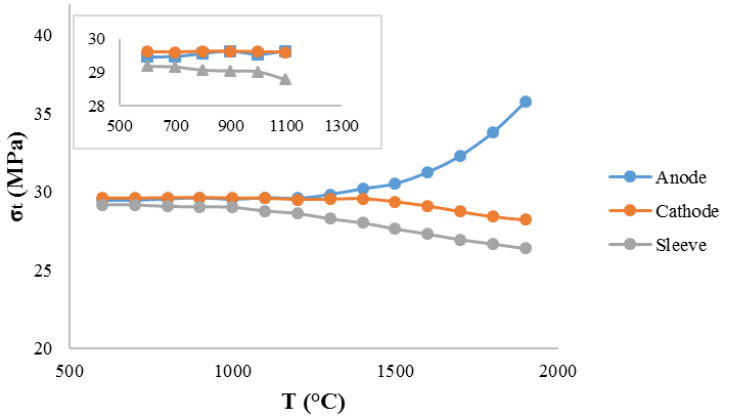

Figure 3. Tensile strengths of anode, cathode and sleeve after the sintering process.

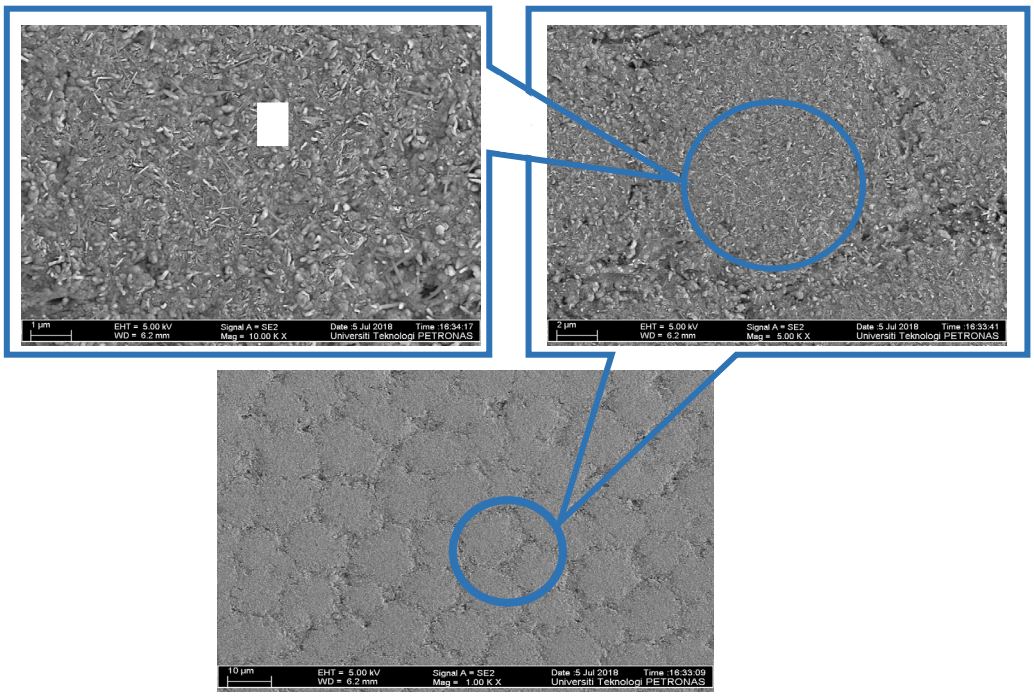

Figure 4. FESEM images of polished sample of lower face of anode.

One of the physical characteristics is XRD which is usually performed for CNTs to get some details about the crystallite size, interlayer space [39], wall numbers and impurities [40]. The XRD pattern of CNTs and graphite have a similarity in the essential features. XRD pattern is helpful to estimate the purity and recognise the microstructural difference between graphite and CNT. The x-ray diffraction profile of graphite presents a sharp peak at diffracted angle 26.3° 2θ, which matches the (002) plane. Besides, the small peaks of graphite are at diffracted angles 42.6°, 44.8°, and 54.2°, which matches the (100), (101) and (004), respectively. At (002) diffracted plane of graphite, the interlayer distancing is 3.3 Å [41]. Figure 5 shows the XRD profile of transformed carbon nanotubes by spark discharge phenomena in this study. CNTs were formed on the lower face of the upper punch (anode) only. The high-intensity peak matches to the (002) diffracted plane locates at diffracted angle 25.86° 2θ which means the difference of diffracted angle between graphite and CNTs at (002) plane is around 0.44°. For these CNTs, the interlayer spacing of plane diffraction of the (002) is 3.4 Å. The average crystallite size of CNTs sample (D_{002}) of 37 nm was estimated from Scherrer's equation. Mainly, CNTs can be divided into four categories which are single wall CNTs, double wall CNTs, few wall CNTs and multiwall

CNTs. The noise and intensity of (002) plane are two crucial differences that can be used to differentiate those categories. For SWCNTs, the noise of (002) plane is the highest, and the intensity is the lowest. But for MWCNTs, the noise of (002) plane is the lowest, and the intensity is the highest because the increase of shell numbers led to an increase in the intensity and decrease in the noise and width of the (002) plane peak [42-45]. Besides, the multilayers spacing of sp2 C=C leads to 2θ downward, as shown in Figure 5. At 42.41° and 43.98°, the (100) and (101) diffraction planes, small peaks of MWCNTs are noticed. This agrees with similar results reported earlier [41, 46].

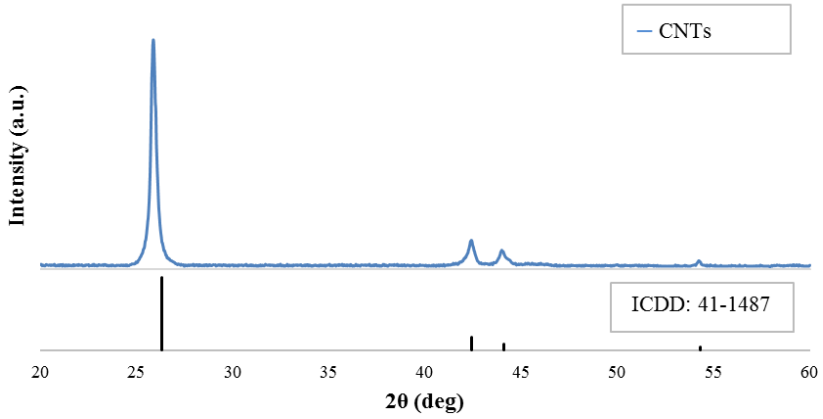

Figure 5. XRD profile of CNTs.

TGA was performed for graphite and CNTs specimens under air atmosphere to 900 °C, at a heating rate of 25 °C/min. Figure 6 shows the TGA curves of CNTs and graphite. The TGA profile of graphite shows a significant weight loss rate at 675 °C because of in-pore diffusion-controlled oxidation, while the oxidation is very slow at a temperature less than 550 °C due to chemical oxidation [47]. Then the weight loss rate reduces at 805 °C. For CNTs, the TGA profile shows higher thermal stability than the graphite [48]. Slightly, the weight loss starts to increase at 645 °C because of the residual graphite that did not transform to CNTs.

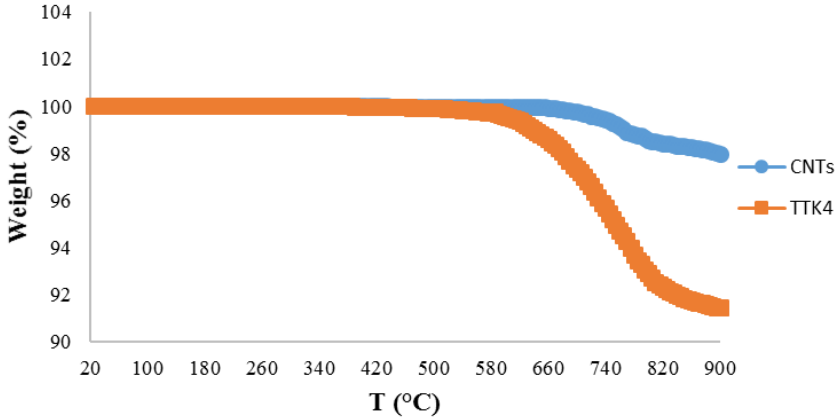

Figure 6. TGA profile of graphite and CNTs

The graphite mould in MCAS apparatus is exposed to the impurity reactants in argon gas during the sintering process and might accidentally expose to oxygen in the air. Since the oxidation rate depends on the temperature, time and type of graphite, the oxidation of graphite must be studied in detail to calculate the mass loss profiles of graphite. Figure 7 shows the variation of mass loss percentages of graphite oxidation with time at different temperatures. For each temperature, the average values of two repeated tests were taken as a result here. The mass losses were estimated from the mass dropped of oxidised graphite samples, and then they were straightened by comparison with the mass of pristine samples (unoxidised sample). Generally, the oxidation rate of graphite is increasing with time and temperature [32]. Sharply, increasing graphite oxidation quantity begins at 1 min for variation temperature when O_2 increased and reached the surface of graphite specimens. At 2 min, all profiles of mass loss percentages of graphite take a linear increase with time and variate with different temperatures. Figure 7 can be divided into three parts based on the oxidation rate at variant temperatures. The first part is below 900 °C. The mass loss percentages are slowly increasing with time which have small slope except the one at 800 °C because it presents the transition from in-pore diffusion-controlled regime to a boundary layer regime. While the mass loss percentages of the first part increase continuously with temperature more than the second and third parts due to the increase in oxidant gas entered the pores with increased temperature led to increasing activation energy. At 8 min, the maximal mass loss percentages of graphite samples at 600 °C, 700 °C and 800 °C are 0.119%, 0.407% and 0.902%, respectively. The second part is between 900 °C and 1400 °C. The extent of mass loss percentage increases with time and the curves from 900 °C to 1400 °C have almost the same slope which is higher than

the slopes of the first part. However, the oxidation based on the increased temperature is lower than the first part due to the decreasing of surface area, and the activation energy is controlled by the boundary layer. At 8 min, the maximal mass loss percentages of graphite samples at 900 °C, 1000 °C, 1100 °C, 1200 °C, 1300 °C and 1400 °C are 1.029%, 1.158%, 1.302%, 1.447%, 1.541% and 1.668% respectively.

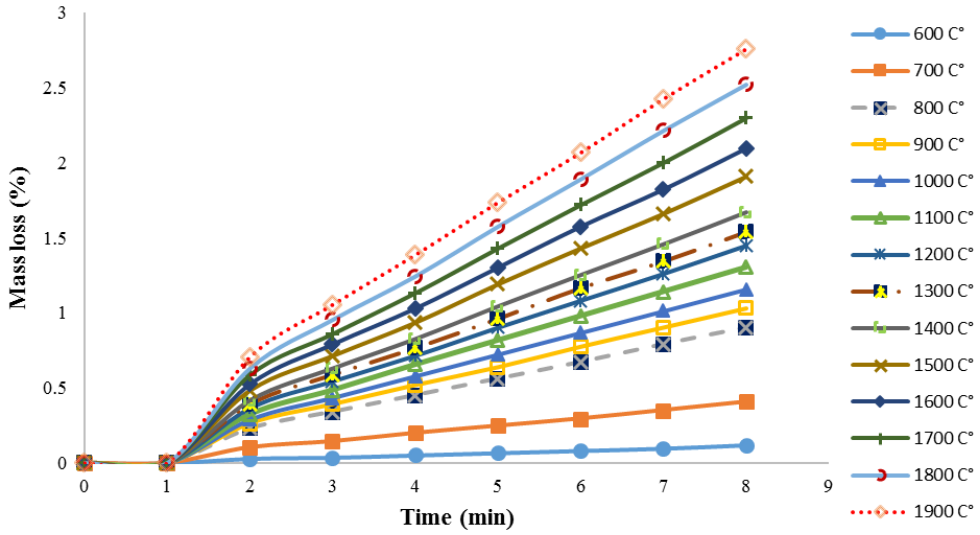

Figure 7. Mass loss percentage of graphite oxidation dependency on time at high temperatures.

The third part is above 1400 °C where the mass loss percentage is greater than others and has the same patterns increasingly. Moreover, the oxidation rate over temperature increases again because of CO production [32], and converting the opened pores to macropores or mesopores would increase superficial surface and accelerate O_2diffusion. At 8 min, the maximal mass loss percentages of graphite samples at 1500 °C, 1600 °C, 1700 °C, 1800 °C and 1900 °C are 1.907%, 2.094%, 2.298%, 2.519% and 2.758% respectively. Owing to the changes in reaction surface, the mass loss percentages are different. For clarifying the behaviour of the graphite oxidation, the oxidation process was done at a constant time. Figure 8 shows the mass loss percentages of graphite specimens at high temperature from 600 °C to 1900 °C at 40 min soaking time. For each temperature, the average values of two repeated tests were taken as a result. At temperature from 600 °C to 800 °C, the mass loss percentage increases greatly and amounts to 5.479% at 800 °C. Then the oxidation rate evens out at 900 °C. At temperatures from 900 °C to 1000 °C, the change in mass loss percentage is very small, around 0.197%. The extent of mass loss percentage again raises at temperatures above 1000 °C. At temperature above 1400 °C, the oxidation quantity is higher than the one at temperatures from 1000 °C to 1400 °C. At 1900 °C, because of the increase in activation energy of oxidation, the maximal mass loss percentage is 14.838%. The change in mass loss rate with temperature expresses different oxidation regimes. Since the change in mass loss percentage leads to a reduction in the strength of graphite structure, the profile of mechanical strength for oxidised graphite was estimated.

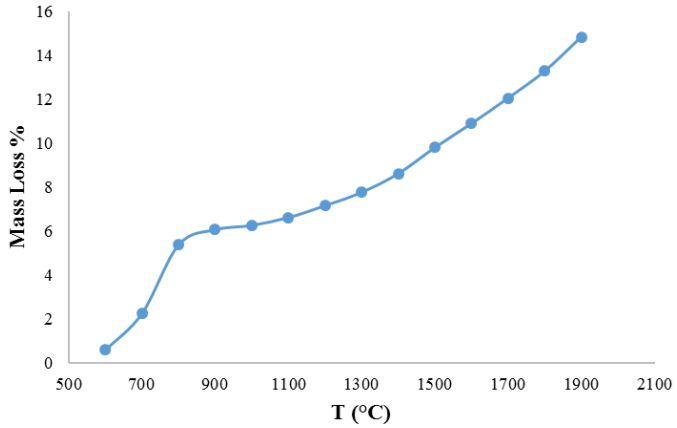

Figure 8. Graphite oxidation at high temperatures.

Figure 9(a) shows the relationship between mass loss percentage of GW-6S graphite and normalised tensile strength, where σ_t represents the tensile strength of pristine graphite sample and $\overline{\sigma_t}$ represents the tensile strength of the oxidised graphite sample. The increase in mass loss percentage of graphite decreases the normalised tensile strength. But, the decrease in normalised tensile strength is higher than the increase in mass loss percentage of graphite. Likely, this is because of the penetration of oxidising gas in the graphite [49] and geometrical reduction. The same behaviour can be found in Figure 9(b), which shows the relationship between mass loss percentage of GW-6S graphite and normalised

compressive strength, but the drop in normalised compressive strength is higher than the normalised tensile strength, where σ_c is the compressive strength of pristine graphite sample, and $\overline{\sigma}_c$ presents the compressive strength of the oxidised graphite sample. Those plots can be helpful to evaluate the tensile and compressive strengths based on mass loss percentage.

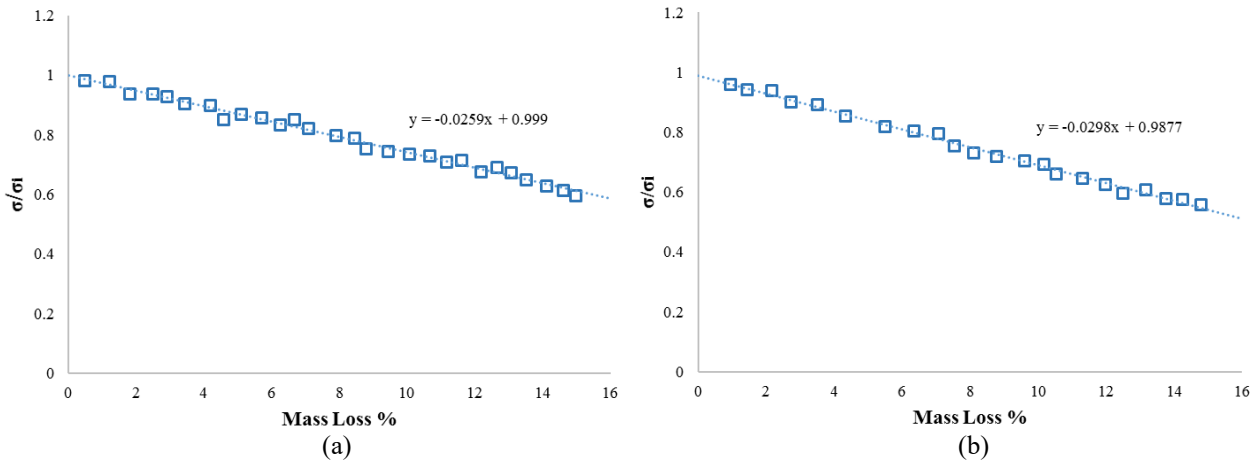

Figure 9. (a) Tensile strength profile and (b) compressive strength profile of oxidised graphite.

CONCLUSION

The effects of MCAS process and oxidation on GW-6S graphite at high temperature of 600-1900 °C were investigated. The graphite transformation to carbon nanotubes is another evidence of spark discharge phenomenon during the MCAS process of nonconductive powder. The tensile strength of the upper punch after sintering process is 20.2% higher than the pristine one because of the transforming of micro-graphite to CNTs which increases with increased temperature. The impurity reactants in argon gas during the sintering process have little influence on the tensile strength of mould components, and the oxidation of graphite sample in the air is higher than the one of CNTs. The variation of mass loss percentages is different due to the difference in control regimes. The decrease in the value of normalised (tensile/compressive) strength is higher than the increase in the value of mass loss percentage of graphite. Besides, the dropping in normalised compressive strength is higher than the normalised tensile strength. Likely, this is because of the penetration of oxidising gas in the graphite and geometrical reduction.

ACKNOWLEDGEMENT

The authors would like to thank Eayn Al-Qitr Sdn. Bhd. for supplying materials, providing access to their SPS equipment, processing knowledge, and assistance in making SPS samples. Research funding from the Universiti Teknologi Petronas, under YUTP-FRG -015LC0-291 is acknowledged and appreciated. Also, they acknowledge the University of Al-Qadisiyah, Iraq, for cooperation to achieve this work.

REFERENCES

[1] Grasso S, Hu C, Maizza G, et al. Effects of pressure application method on transparency of spark plasma sintered alumina. Journal of the American Ceramic Society 2011; 94(5): 1405-1409.

[2] Albarody TMB, Al-Jothery HKM, Hussein AR, et al. Ultrafast-contactless plasma arc sintering. AIP Conference Proceedings 2018; 2035: 080008

[3] Cologna M, Rashkova B, Raj R. Flash sintering of nanograin zirconia in< 5 s at 850 C. Journal of the American Ceramic Society 2010; 93(11): 3556-3559.

[4] Zhou Y, Hirao K, Toriyama M, Tanaka H. Very rapid densification of nanometer silicon carbide powder by pulse electric current sintering. Journal of the American Ceramic Society 2000; 83(3): 654-656.

[5] Giuntini D, Raethel J, Herrmann M, et al. Spark plasma sintering novel tooling design: Temperature uniformisation during consolidation of silicon nitride powder. Journal of the Ceramic Society of Japan 2016; 124(4): 403-414.

[6] Bennett C, McKinnon N, Williams L. Sintering in gas discharges. Nature 1968; 217(5135): 1287-1288.

[7] Johnson DL. Microwave and plasma sintering of ceramics. Ceramics International 1991; 17(5): 295-300.

[8] Li C, Li S, An D, Xie Z. Microstructure and mechanical properties of spark plasma sintered SiC ceramics aided by B4C. Ceramics International 2020; 46(8): 10142-10146.

[9] Hashiguchi H, Kinugasa H. Electrical resistivity of α-sic ceramics added with NiO. Journal of the Ceramic Society of Japan 1994; 102(1182): 160-164.

[10] Anselmi-Tamburini U, Garay J, Munir Z, et al. Spark plasma sintering and characterisation of bulk nanostructured fully stabilised zirconia: Part I. Densification studies. Journal of Materials Research 2004; 19(11): 3255-3262.

[11] Anselmi-Tamburini U, Garay J, Munir Z, et al. Spark plasma sintering and characterisation of bulk nanostructured fully stabilised zirconia: Part II. Characterisation studies. Journal of Materials Research 2004; 19(11): 3263-3269.

[12] Al-Jothery H, Albarody T, Yusoff P, et al. A review of ultra-high temperature materials for thermal protection system. IOP Conference Series: Materials Science and Engineering 2020; 863: 012003.

[13] Guillon O, Gonzalez-Julian J, Dargatz B, et al. Field-assisted sintering technology/spark plasma sintering: Mechanisms, materials, and technology developments. Advanced Engineering Materials 2014; 16(7): 830-849.

[14] Omori M. Sintering, consolidation, reaction and crystal growth by the spark plasma system (SPS). Materials Science and Engineering: A 2000; 287(2): 183-188.

[15] Munir Z, Anselmi-Tamburini U, Ohyanagi M. The effect of electric field and pressure on the synthesis and consolidation of materials: A review of the spark plasma sintering method. Journal of Materials Science 2006; 41(3): 763-777.

[16] Anselmi-Tamburini U, Gennari S, Garay J, Munir ZA. Fundamental investigations on the spark plasma sintering/synthesis process: Ii. Modeling of current and temperature distributions. Materials Science and Engineering: A 2005; 394(1-2): 139-148.

[17] Sonber J, Murthy TC, Subramanian C, et al. Investigations on synthesis of ZrB2 and development of new composites with HFB2 and TiSi2. International Journal of Refractory Metals and Hard Materials 2011; 29(1): 21-30.

[18] Rangaraj L, Divakar C, Jayaram V. Fabrication and mechanisms of densification of zrb2-based ultra high temperature ceramics by reactive hot pressing. Journal of the European Ceramic Society 2010; 30(1): 129-138.

[19] Ma R, Wu J, Wei B, et al. Processing and properties of carbon nanotubes–nano-sic ceramic. Journal of materials science 1998; 33(21): 5243-5246.

[20] Deepak D, Shrinivas P, Hemant G, Iasy R. Optimisation of current and pulse duration in electric discharge drilling of D2 steel using graphite electrode. International Journal of Automotive and Mechanical Engineering 2018; 15(4): 5914-5926.

[21] Azizir-Rahim M, Yusop MZ, Othman M, et al. In situ transmission electron microscope: Joule heating effect on graphitisation of copper incorporated carbon nanofiber. International Journal of Automotive and Mechanical Engineering 2019; 16(3): 6931-6939.

[22] Widmann R. International society for rock mechanics commission on rock grouting. International Journal of Rock Mechanics and Mining Sciences & Geomechanics Abstracts 1996; 33(8): 803-847.

[23] Grasso S, Kim BN, Hu C, et al. Highly transparent pure alumina fabricated by high-pressure spark plasma sintering. Journal of the American Ceramic Society 2010; 93(9): 2460-2462.

[24] Grasso S, Yoshida H, Porwal H, et al. Highly transparent α-alumina obtained by low cost high pressure SPS. Ceramics International 2013; 39(3): 3243-3248.

[25] Luo X, Yu X, Yu S. Oxidation performance of graphite material in reactors. Frontiers of Energy and Power Engineering in China 2008; 2(4): 471-474.

[26] Heintz E, Parker W. Catalytic effect of major impurities on graphite oxidation. Carbon 1966; 4(4): 473-482.

[27] Ambrosi A, Chua CK, Khezri B, et al. Chemically reduced graphene contains inherent metallic impurities present in parent natural and synthetic graphite. Proceedings of the National Academy of Sciences 2012; 109(32): 12899-12904.

[28] Zhang X, Yi Y, Zhu H, et al. Measurement of tensile strength of nuclear graphite based on ring compression test. Journal of Nuclear Materials 2018; 511: 134-140.

[29] Li D-y, Tao W, Cheng T-j, Sun X-l. Static and dynamic tensile failure characteristics of rock based on splitting test of circular ring. Transactions of Nonferrous Metals Society of China 2016; 26(7): 1912-1918.

[30] Al-Jothery H, Albarody T, Yusoff P, et al. Crashworthiness design for trapezoid origami crash structure numerical. International Journal of Automotive and Mechanical Engineering 2020; 17(1): 7667-7674.

[31] Al-Jothery HKM, Yusoff PSM, Albarody TMB, Balakrishnan VK. Fabrication of flexible ep-fg composite automobile shell structure using compression moulding process. Platform: A Journal of Engineering 2019; 3(2): 22-32.

[32] Xiaowei L, Jean-Charles R, Suyuan Y. Effect of temperature on graphite oxidation behavior. Nuclear Engineering and design 2004; 227(3): 273-280.

[33] Krinitsyn A, Pazukhin E. Graphite specimens from the fourth block of the Chernobyl atomic energy station. Ii. Kinetics of graphite oxidation. Radiochemistry 1995; 36(6).

[34] Prasek J, Drbohlavova J, Chomoucka J, et al. Methods for carbon nanotubes synthesis. Journal of Materials Chemistry 2011; 21(40): 15872-15884.

[35] Hammood HS, Irhayyim S, Awad A, Abdulhadi H. Influence of multiwall carbon nanotube on mechanical and wear properties of copper–iron composite. International Journal of Automotive and Mechanical Engineering 2020; 17(1): 7570-7576.

[36] Gugulothu S, Pasam VK. Performance evaluation of CNT/MoS2 hybrid nanofluid in machining for surface roughness. International Journal of Automotive and Mechanical Engineering 2019; 16(4): 7413-7429.

[37] Arora N, Sharma N. Arc discharge synthesis of carbon nanotubes: Comprehensive review. Diamond and Related Materials 2014; 50: 135-150.

[38] Zhang C, Song Y, Zhang H, et al. Mechanical properties of carbon nanotube fibers at extreme temperatures. Nanoscale 2019; 11(10): 4585-4590.

[39] Belin T, Epron F. Characterization methods of carbon nanotubes: A review. Materials Science and Engineering: B 2005; 119(2): 105-118.

[40] Futaba DN, Yamada T, Kobashi K, et al. Macroscopic wall number analysis of single-walled, double-walled, and few-walled carbon nanotubes by x-ray diffraction. Journal of the American Chemical Society 2011; 133(15): 5716-5719.

[41] Mohammad M, Moosa AA, Potgieter J, Ismael MK. Carbon nanotubes synthesis via arc discharge with a yttria catalyst. International Scholarly Research Notices 2013; 2013: 1-7.

[42] Mhamane D, Ramadan W, Fawzy M, et al. From graphite oxide to highly water dispersible functionalised graphene by single step plant extract-induced deoxygenation. Green Chemistry 2011; 13(8): 1990-1996.

[43] Tang Y, Huang F, Zhao W, et al. Synthesis of graphene-supported Li4Ti5O12 nanosheets for high rate battery application. Journal of Materials Chemistry 2012; 22(22): 11257-11260.

[44] Boccaleri E, Arrais A, Frache A, et al. Comprehensive spectral and instrumental approaches for the easy monitoring of features and purity of different carbon nanostructures for nanocomposite applications. Materials Science and Engineering: B 2006; 131(1-3): 72-82.

[45] Lee CY, Bae J-H, Kim T-Y, et al. Using silane-functionalised graphene oxides for enhancing the interfacial bonding strength of carbon/epoxy composites. Composites Part A: Applied Science and Manufacturing 2015; 75: 11-17.

[46] Li H, Liu C, Fan S. Homogeneous carbon nanotube/carbon composites prepared by catalysed carbonisation approach at low temperature. Journal of Nanomaterials 2011; 2011: 1-5.

[47] Lee J, Won S, Shim J, et al. Electrochemical characteristics of silicon-carbon composite anodes for lithium rechargeable batteries. Transactions on Electrical and Electronic Materials 2014; 15(4): 193-197.

[48] Salam MA, Burk R. Synthesis and characterisation of multi-walled carbon nanotubes modified with octadecylamine and polyethylene glycol. Arabian Journal of Chemistry 2017; 10: S921-S927.

[49] Ishihara M, Sumita J, Shibata T, et al. Principle design and data of graphite components. Nuclear Engineering and design 2004; 233(1-3): 251-260.